Zhang *et al. Energy Mater* 2024;4:400028
DOI: 10.20517/energymater.2023.101

Energy Materials

Article

Open Access

Check for updates

NiFe Prussian blue analog cocatalyzed TiO_2/In_2S_3 type-II heterojunction for solar water splitting

Ming Zhang[1], Pingping Yang[2], Wenyan Tao[3], Xiangui Pang[2], Youyi Su[2], Pai Peng[2], Lin Zheng[2], Runhan Li[2], Shuxiang Wang[2], Jing Huang[2], Li Zou[2], Jiale Xie[2,*]

[1]School of Chemistry and Chemical Engineering, Southwest Petroleum University, Chengdu 610500, Sichuan, China.
[2]School of New Energy and Materials, Southwest Petroleum University, Chengdu 610500, Sichuan, China.
[3]Tongwei Solar Company, Chengdu 610299, Sichuan, China.

***Correspondence to:** Dr. Jiale Xie, School of New Energy and Materials, Southwest Petroleum University, 8 Xindu Road, Xindu District, Chengdu 610500, Sichuan, China. E-mail: jialexie@swpu.edu.cn

How to cite this article: Zhang M, Yang P, Tao W, Pang X, Su Y, Peng P, Zheng L, Li R, Wang S, Huang J, Zou L, Xie J. NiFe Prussian blue analog cocatalyzed TiO_2/In_2S_3 type-II heterojunction for solar water splitting. *Energy Mater* 2024;4:400028. https://dx.doi.org/10.20517/energymater.2023.101

Received: 11 Dec 2023 **First Decision:** 5 Mar 2024 **Revised:** 20 Mar 2024 **Accepted:** 28 Mar 2024 **Published:** 3 Apr 2024

Academic Editors: Sining Yun, Nicolas Alonso-Vante **Copy Editor:** Fangling Lan **Production Editor:** Fangling Lan

Abstract

Due to the excellent stability of titanium dioxide (TiO_2), there is still value in improving its solar-to-hydrogen conversion efficiency through tremendous attempts. Metal sulfides with a narrow bandgap are good candidates to broaden the ultraviolet light absorption of TiO_2 into the visible light region. However, sulfides suffer from the photocorrosion issue, leading to poor stability. Herein, a type-II heterojunction of TiO_2/In_2S_3 is fabricated by a hydrothermal method, and a NiFe Prussian blue analog (NFP) overlayer is deposited on the surface of TiO_2/In_2S_3 through a chemical bath deposition technique. Under AM1.5G illumination, a photocurrent density of 1.81 mA cm^{-2} can be obtained with NFP coated TiO_2/In_2S_3 at 1.23 V *vs.* reversible hydrogen electrode, which is six folds of the photocurrent of TiO_2. This photocurrent value can reach up to about 90% of its theoretical photocurrent. During a 12 h stability test, the TiO_2/In_2S_3/NFP photoanode exhibits a high photocurrent retention of 95.17% after an initial transient decrease. The type-II heterojunction of TiO_2/In_2S_3 can efficiently boost the charge separation because of the built-in electric field and enhance the visible-light absorption because of the narrow bandgap of In_2S_3. A NFP overlayer serves as the cocatalyst for water oxidation reaction due to its valence changes of nickel and iron elements. NFP cocatalyst can rapidly extract the photogenerated holes from In_2S_3 and then improve the charge separation/injection efficiencies. Thanks to chemical stability of NFP, its coating can also make In_2S_3 resistant to photocorrosion by physically separating the photoanode from the electrolyte. Therefore, there is a good synergistic effect between the TiO_2/In_2S_3 heterojunction and NFP cocatalyst. This work provides some crucial insights for the interface engineering and material design in photoelectrochemical systems.

Keywords: Solar water splitting, heterojunction, cocatalyst, Prussian blue analog, indium sulfide

INTRODUCTION

Green hydrogen produced through solar water splitting is a promising and sustainable approach. There is no carbon footprint in the whole procedure. Photoelectrochemical (PEC) water splitting is one of the solar water splitting techniques, which has moderate solar-to-hydrogen efficiency and system complexity in comparison with photocatalysis and photovoltaic-electrolysis strategies[1,2]. The efficiency of PEC water splitting is still lower than the expected efficiency of 10%. A photoanode is a crucial limit component in one PEC device due to the sluggish kinetics of water oxidation reaction[3]. Among various *n*-type semiconductors for photoanodes, titanium dioxide (TiO_2) is a good candidate, which possesses excellent PEC stability and unique electronic properties[4]. However, its PEC performance is limited by the fast charge recombination and the low light absorption[5]. Several strategies have been developed to improve the charge separation and suppress the charge recombination, such as doping[6-8], nanostructuring[9-11], cocatalyst modification[12-14], and heterojunction construction[15-17]. Constructing heterojunction is a widely accepted approach to enhance the charge separation with other semiconductors such as TiO_2[15,18] and $BiVO_4$[19]. However, it is hard to construct a type-II heterojunction with other semiconductors due to large bandgaps of TiO_2.

The III-VI group chalcogenide semiconductors have recently received great attention due to their narrow bandgaps. Among the metal sulfides, indium sulfide (In_2S_3) has a bandgap of 2.0-2.3 eV, a high absorption coefficient, excellent conductivity, and low toxicity. Park *et al.* fabricated S, N-doped TiO_2/In_2S_3 heterojunction and obtained a high photocurrent density of 2.73 mA cm^{-2} at 1.23 V *vs.* reversible hydrogen electrode (RHE), while S, N-doped TiO_2 shows a photocurrent density of 1.93 mA cm^{-2}[20]. However, the charge injection efficiency of TiO_2/In_2S_3 was not improved compared to TiO_2 photoanodes. This suggests the photogenerated holes would be accumulated on the surface of In_2S_3. Therefore, cocatalyst should be introduced to improve the charge injection efficiency from the photoanode to water molecules. Commonly used cocatalyst materials for this purpose include noble metals (such as Au and Pt)[21], phosphates[22], layered double hydroxides (LDH)[23], and Prussian blue analogs (PBAs)[24,25]. PBAs, a category of mixed-valence compounds, are characterized by a structure composed of two distinct or identical metal ions connected through cyanide bonds within a face-centered cubic (FCC) framework. They are considered chemically stable due to the strength of cyanide bridging, active in a wide pH range, and non-toxic. CoFe PBAs have been broadly used to modify $BiVO_4$[26,27], Fe_2O_3[28], Fe_2O_3/Fe_2TiO_5[24], TiO_2[29], and Sb:TiO_2[30]. Further, a phosphate ions layer was inserted between Fe_2O_3 and CoFe PBA to drift the migration of photogenerated holes[31]. Hybrid CuFe-CoFe PBAs were also developed to modify $BiVO_4$[32]. The cocatalytic effects of NiFe PBAs (NFP) have been investigated on the photoanodes of Zr-doped $BiVO_4$[33] and ZnO/$BiVO_4$[34]. All the reported results indicate that PBAs can improve the photocurrent and/or lower the onset potential of photoanodes. The probable mechanism is attributed to the formation of a favorable interface for efficient hole transfer and the catalytic activity of PBAs. Considering the photocorrosion of In_2S_3, the accumulated holes can break the In-S bond or attack S^{2-} ions and then oxidize In_2S_3 rather than H_2O[35]. Thereby, the In_2S_3 sulfide was decomposed into the soluble sulfate. Thanks to the excellent chemical stability of PBAs, it can be strongly expected that the PBAs coated TiO_2/In_2S_3 heterojunction would possess a good PEC stability combined with an enhanced photocurrent.

In this work, a type-II heterojunction of TiO_2/In_2S_3 was first fabricated by a hydrothermal strategy. NFP catalyst was then grown on the surface of the TiO_2/In_2S_3 heterojunction through a chemical bath technique. The ternary TiO_2/In_2S_3/NFP photoanode shows a high photocurrent of 1.81 mA cm^{-2} at a potential of 1.23 V *vs.* RHE, which is six folds of the photocurrent of 0.30 mA cm^{-2} observed with the TiO_2 photoanode. Based on the ultraviolet-visible (UV-vis) absorption spectroscopy of a TiO_2/In_2S_3/NFP photoanode, the maximum

achievable photocurrent is 2.03 mA cm^{-2}. Therefore, there is a narrow gap between theoretical value and experimental value in this work. The charge injection efficiency and charge separation efficiency can reach up to 93.86% and 93.55% with TiO_2/In_2S_3/NFP, respectively. After an initial transient decrease of the photocurrent, the TiO_2/In_2S_3/NFP photoanode obtained a high photocurrent retention of 95.17% after a 12 h stability test. Thus, we fabricated a ternary TiO_2/In_2S_3/NFP photoanode with a high photocurrent and good stability simultaneously. The detailed material characterizations, PEC performance measurements, and probable mechanism will be discussed below.

EXPERIMENTAL

Preparation of TiO_2, TiO_2/In_2S_3, and TiO_2/In_2S_3 /NFP

All reagents were purchased from Aladdin and were used as received without further purification. Deionized water (DI, ~18.25 MΩ cm) was used during the experiments.

Preparation of TiO_2: The fabrication of TiO_2 nanorod arrays was accomplished using a reported hydrothermal method with some modifications[36]. Fluorine-doped tin dioxide conductive glass substrates (FTO, 2.5 cm × 1 cm, sheet resistance < 10 Ω sq^{-1}) were ultrasonically cleaned in acetone, ethanol and DI sequentially for 30 min each. FTO glasses were dried with a N_2 gas flow before use. To prepare the precursor, 20 mL of the concentrated HCl (38%) was dropped into 20 mL DI water. Then, 668 μL of titanium isopropoxide was infused into the above solution. The resulting solution was subsequently transferred into a 50 mL Teflon-lined stainless steel autoclave. FTO substrates were gently placed in the autoclave at an angle, ensuring that its conductive sides faced downward. Hydrothermal reactions were performed at 170 °C for 6 h. Following this, the samples underwent annealing in air at 350 °C for 1 h, with a heating rate of 5 °C min^{-1}.

Preparation of TiO_2/In_2S_3: To obtain the TiO_2/In_2S_3 heterojunction, In_2S_3 was hydrothermally grown on the as-prepared TiO_2. The indium nitrate and thioacetamide were dissolved into the DI water of 40 mL with a stoichiometric ratio of 1:3. The amount of indium nitrate was set at 0.05, 0.1, 0.2, and 0.3 millimoles. TiO_2 was carefully placed in an autoclave with the film surface facing downward. Subsequently, the autoclave was subjected to a hydrothermal procedure at 180 °C for 12 h. After the autoclave had cooled to room temperature, the samples were taken out and washed with DI water. The samples were then transferred to a tube furnace, where they underwent annealing at 350 °C for 30 min under a nitrogen atmosphere. Based on the amount of indium nitrate used in the precursor, the TiO_2/In_2S_3 samples are labeled as TiO_2/In_2S_3-x.

Preparation of TiO_2/In_2S_3/NFP: A layer of NiFe Prussian blue (NFP) was deposited on the surface of TiO_2/In_2S_3 via a chemical bath method[24]. Firstly, 0.02 M $Ni(NO_3)_2 \cdot 6H_2O$ and 0.02 M $K_3Fe(CN)_6$ were mixed under vigorous stirring. After that, TiO_2/In_2S_3 was immersed in the above solution. The optimal temperature for NFP growth is 60 °C. The optimal reaction time is 3 h. After the growth of NFP, the samples were washed with DI water and then dried overnight in a 60 °C oven.

PEC performance measurements

PEC performance tests were performed using a three-electrode system with an electrochemical workstation (CHI 660E). TiO_2/In_2S_3/NFP photoanodes were used as the working electrode; an Ag/AgCl electrode was used as the reference electrode, and a platinum wire was used as the counter electrode. The photoanodes were irradiated with the AM1.5G solar spectrum with an intensity of 100 mW cm^{-2} (CELHXF 300). Additionally, 1 M KOH aqueous solution (pH = 13.6) was employed as the electrolyte. Linear sweep voltammetry (LSV) measurements were performed at a scan rate of 20 mV s^{-1} with a potential range of 0-1.4 V *vs.* RHE. The PEC impedance spectroscopy (PEIS) was recorded at a potential of 0.47 V *vs.* RHE

with a perturbation of 10 mV under AM1.5 illumination. The frequency range is from 0.1 to 10^5 Hz. The obtained PEIS plots were fitted using Z-View software. Mott-Schottky (M-S) measurements were conducted in the dark at a fixed frequency of 2,000 Hz. Donor density (N_D) and flat-band potential (V_{fb}) can be obtained from the M-S equation, denoted as:

$$\frac{1}{C^2} = \frac{2}{(\varepsilon\varepsilon_r A^2 e N_D)}\left(V\text{-}V_{fb}\text{-}\frac{K_b T}{e}\right) \quad (1)$$

In this study, the variables are defined as follows: A (electrode area), C (space charge capacitance), V (the applied potential), ε (dielectric constant with a value of 8.85×10^{-12} F m^{-1}), ε_r (vacuum dielectric constant, $\varepsilon_r = 100$), e (elementary charge), K_b (Boltzmann constant with a value of 1.38×10^{-23} J K^{-1}), and T (temperature).

To evaluate the charge separation efficiency (η_{sep}) and charge injection efficiency (η_{inj}), a mixed electrolyte comprising 1 M KOH and 0.5 M Na_2SO_3 was employed. The calculation formulas for η_{inj} and η_{sep} are established as:

$$\eta_{sep} = J_{Na_2SO_3}/J_{abs} \quad (2)$$

$$\eta_{inj} = J_{H_2O}/J_{Na_2SO_3} \quad (3)$$

The current density of J_{H_2O} was measured in 1 M KOH, while the current density of $J_{Na_2SO_3}$ was measured in the presence of a sacrificial agent containing 0.5 M Na_2SO_3. J_{abs} represents the theoretical photocurrent density calculated based on light absorption, which is calculated based on the UV-vis absorption spectra of the photoanodes.

The transformation from the measured potential ($E_{Ag/AgCl}$) to the potential versus reversible hydrogen electrode (E_{RHE}) is dictated by:

$$E_{RHE} = E_{Ag/AgCl} + 0.1971\ \text{V} + 0.0591\ pH \quad (4)$$

The electrochemical active surface area (ECSA) is typically quantified using the double-layer capacitance measured by cyclic voltammetry (CV). The magnitude of C_{dl} is calculated to assess the ECSA of the photoanodes. The formula for calculating ECSA is provided as:

$$C_{dl} = \Delta J/\Delta E \quad (5)$$

$$ECSA = C_{dl}/C_s \quad (6)$$

Where C_{dl} represents the electrochemical double-layer capacitance, ΔJ is the recorded current density variation during the potential scan, and ΔE is the corresponding potential change. C_s signifies the specific capacitance, which is considered constant within the same electrolyte.

The transient decay time (τ) is calculated by:

$$D = \frac{I_t\text{-}I_s}{I_{in}\text{-}I_s} \quad (7)$$

where I_t represents the photocurrent at time t, I_s denotes the photocurrent at steady state, and I_{in} signifies the photocurrent of the anodic spike. The time at which lnD = -1 is designated as the transient decay time (τ).

Materials characterizations

The crystal structure was investigated using an X-ray diffractometer (XRD, Rigaku Ultima IV, Japan) with a Cu K_α radiation source. Field-emission scanning electron microscopy (FESEM, thermo scientific Apreo 2C, Thermo Fisher) and energy-dispersive X-ray spectroscopy (EDS) were employed for morphological observations and compositional analysis of the prepared photoanodes. Transmission electron microscopy (TEM) was used to obtain atomic-resolution images (TEM, Talos F200S G2 instrument, USA). UV-vis absorption spectra of TiO_2-based photoanodes were recorded in the wavelength range of 300-800 nm (Shimadzu UV-3600 Plus), while the UV-vis absorption spectra of In_2S_3 powder samples were measured on Lambda 1050 UV-Vis-NIR spectrophotometer. Surface elemental information of the samples was obtained using X-ray photoelectron spectroscopy (XPS, Escalab Xi$^+$, Thermo Fisher). Ultraviolet photoelectron spectroscopy (UPS, Escalab Xi$^+$, Thermo Fisher) and He I (21.22 eV) photon source were employed to obtain information about binding energies. The UPS spectra were analyzed to derive the valence bands (VB) and work functions of the photoanodes. Photoluminescence spectra (PL, Edinburgh FLS980) were obtained under ambient and unbiased conditions with an excitation wavelength of 425 nm.

RESULTS AND DISCUSSION

Properties of TiO_2/In_2S_3/NFP

The morphology of TiO_2-based photoanodes was characterized first. Figure 1A-C shows the top-view SEM images of TiO_2, TiO_2/In_2S_3, and TiO_2/In_2S_3/NFP. Figure 1D-F displays the cross-sectional SEM images correspondingly. As shown in Figure 1A and D, we successfully synthesized ordered, vertically aligned TiO_2 nanorod arrays on FTO substrates, with a diameter of approximately 0.15 μm and a length of 2.3 μm. In_2S_3 nanosheets assembled nanostructures can be clearly observed on the surface of TiO_2 nanorods in Figure 1B and E. Cross-sectional EDS mappings of TiO_2/In_2S_3 in Supplementary Figure 1A and B indicate that the coating of In_2S_3 is uniform in the whole TiO_2 film. After the growth of NFP, the surface of TiO_2/In_2S_3 is completely covered with NFP nanoparticles [Figure 1C and F]. As illustrated in Supplementary Figure 1C and D, Fe, Ni, C, and N elements are evenly distributed within the film thickness. EDS pattern of TiO_2/In_2S_3/NFP is shown in Supplementary Figure 2. The mass percentages of TiO_2, In_2S_3, and NFP calculated roughly from EDS pattern are ~70.13%, ~2.86%, and ~2.78%, respectively. Figure 1G and H presents TEM images of TiO_2/In_2S_3 and TiO_2/In_2S_3/NFP, respectively. In_2S_3 exhibits a nanosheet-like structure growing on the surface of TiO_2 nanorods, while NFP nanoparticles appear to cover the TiO_2/In_2S_3 heterojunction. Some sheet-like In_2S_3 nanostructures can also be observed in Figure 1H, suggesting that the growth of NFP did not significantly affect the structure of In_2S_3. In Figure 1I, a high-resolution TEM (HRTEM) image of TiO_2/In_2S_3/NFP shows the formation of heterojunction among TiO_2, In_2S_3, and NFP. Moreover, NFP nanoparticles exhibit a low crystallinity. Figure 1J and K presents an HRTEM image and selected area electron diffraction (SAED) on the TiO_2 region. The interplanar spacings are measured as $d_{(110)}$ = 0.322 nm and $d_{(101)}$ = 0.237 nm, corresponding to the tetragonal rutile phase of TiO_2. Figure 1L and M exhibits HRTEM and SAED on the region of In_2S_3. The lattice spacings of $d_{(103)}$ = 0.621 nm and $d_{(109)}$ = 0.33 nm illustrate that the synthesized In_2S_3 is β-In_2S_3 with a tetragonal phase. β-In_2S_3 has a defective spinel structure with the In^{3+} vacancies, which leads to the n-type characteristics of In_2S_3[35].

XRD patterns shown in Figure 2A reveal the crystal structure of TiO_2, TiO_2/In_2S_3, and TiO_2/In_2S_3/NFP. Some XRD peaks from the FTO substrate are marked with stars. The XRD peaks from the TiO_2 film can be well attributed to the rutile phase of TiO_2 (JCPDS No. 21-1276). The XRD peaks at 14.25, 27.43, 33.23, and 47.7° can be attributed to the (103), (109), (0012), and (2212) crystal planes of β-In_2S_3 (JCPDS No. 25-0390). Two XRD peaks at 17.3 and 24.57° correspond to the (200) and (220) crystal planes of $NiFe(CN)_6$ (JCPDS

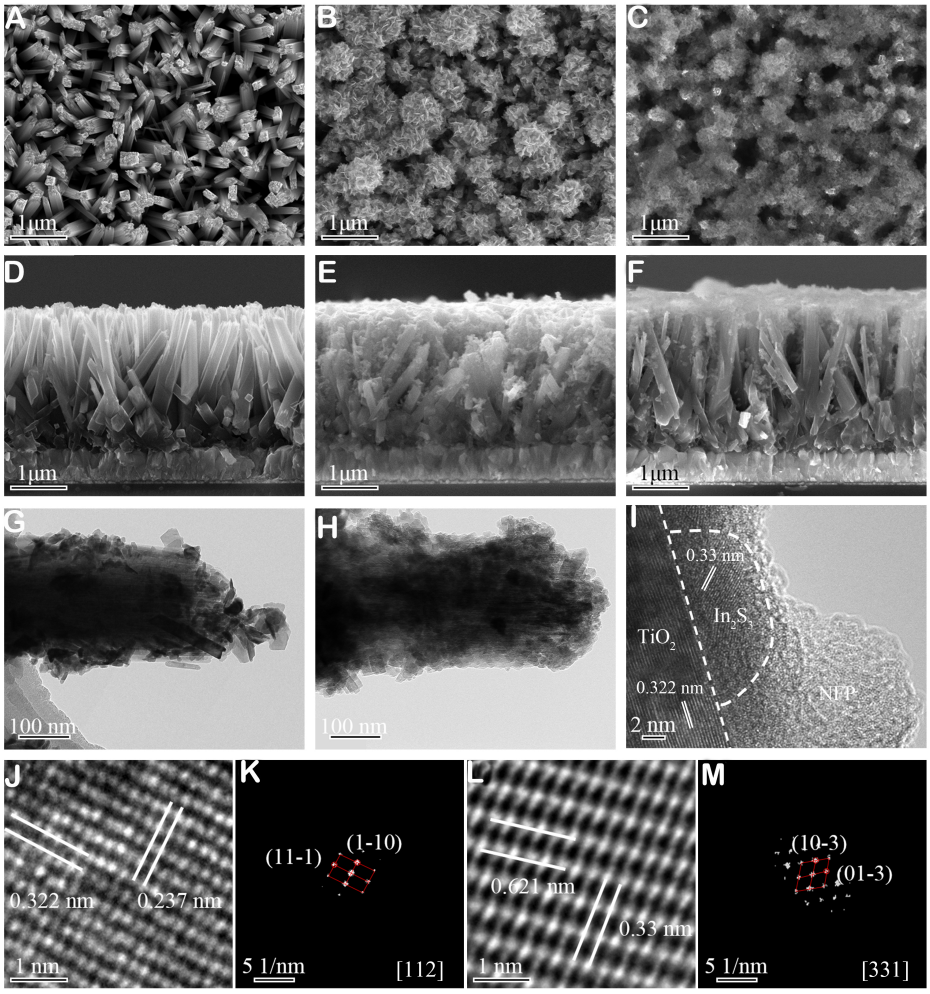

Figure 1. Morphology characterizations of TiO_2-based photoanodes. (A-C) SEM images of TiO_2, TiO_2/In_2S_3, and TiO_2/In_2S_3/NFP. (D-F) Cross-sectional SEM images of TiO_2, TiO_2/In_2S_3, and TiO_2/In_2S_3/NFP. (G) TEM image of TiO_2/In_2S_3. (H) TEM image of TiO_2/In_2S_3/NFP. (I) HRTEM image of TiO_2/In_2S_3/NFP. (J and K) HRTEM and SAED of TiO_2 region. (L and M) HRTEM and SAED of In_2S_3 region.

No. 51-1897), respectively. Moreover, the XRD peaks of In_2S_3 can also be observed on the photoanode of TiO_2/In_2S_3/NFP, suggesting the crystal structure of In_2S_3 is unaffected[37].

The composition and chemical states of the TiO_2-based photoanodes were analyzed with XPS, as presented in Supplementary Figure 3 and Figure 2B-H. All elements of Ti, O, S, In, Ni, Fe, N, and C were successfully identified on the XPS survey spectra. In Figure 2B, Ti $2p_{1/2}$ and Ti $2p_{3/2}$ peaks can be observed at 458.6 and 464.3 eV on the TiO_2 photoanode, respectively. No other peaks were observed at lower binding energy, indicating only the presence of Ti^{4+}, not Ti^{3+}[38]. For TiO_2/In_2S_3, Ti $2p_{1/2}$ and Ti $2p_{3/2}$ peaks show a positive shift of 0.4 eV compared to the as-prepared TiO_2. In Figure 2C, O 1s XPS spectra can be fitted with two peaks corresponding to Ti-O and oxygen vacancies (O_v)/S-O. The Ti-O peak also shows a positive shift of 0.35 eV after the growth of In_2S_3. It is important to mention that the S-O peak overlaps with the O_V peak due to similar binding energies[20,39]. In Figure 2D, the S 2p XPS spectra of In_2S_3 powder exhibit two peaks at 161.61 and 162.82 eV, corresponding to the S $2p_{3/2}$ and S $2p_{1/2}$ peaks, respectively. After the formation of TiO_2/In_2S_3 heterojunction, these two peaks display a negative shift of ~0.15 eV. The opposite shift direction of Ti 2p/O 1s and S 2p powerfully demonstrates the charge transfer from TiO_2 to In_2S_3 at the heterojunction

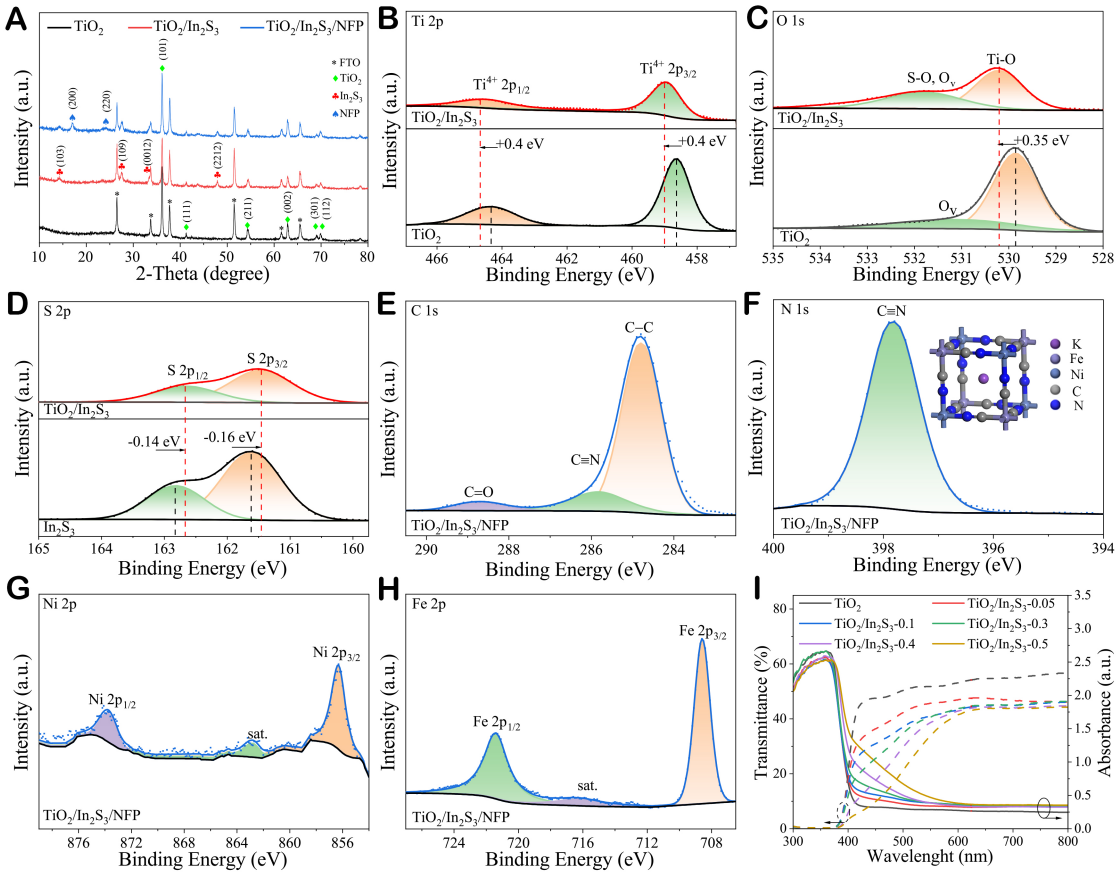

Figure 2. (A) XRD patterns of TiO_2, TiO_2/In_2S_3, and TiO_2/In_2S_3/NFP. XPS spectra of (B) Ti 2p, (C) O 1s, and (D) S 2p of TiO_2/In_2S_3. XPS spectra of (E) C 1s, (F) N 1s, (G) Ni 2p, and (H) Fe 2p of TiO_2/In_2S_3/NFP. Inset of (F): the crystal structure of NiFe PBA. (I) Transmission spectra and UV-vis absorption spectra of TiO_2 and TiO_2/In_2S_3 with the different concentrations of indium nitrate in the precursor.

interface and the formation of a built-in electric field oriented from TiO_2 to In_2S_3[16]. The C 1s spectrum of TiO_2/In_2S_3/NFP in Figure 2E can be deconvoluted into three distinct peaks located at 284.8 (C-C), 285.8 (C≡N), and 288.6 eV (C=O). The N 1s spectrum of TiO_2/In_2S_3/NFP depicted in Figure 2F confirms the presence of C≡N at 397.8 eV. The crystal structure of NFP is shown in the inset of Figure 2F. This demonstrates that the covering of NFP on the surface of TiO_2/In_2S_3 heterojunction is successful. In Figure 2G, the peaks located at binding energies of 873.8 and 856.3 eV correspond to the Ni $2p_{1/2}$ and Ni $2p_{3/2}$ peaks, respectively. The Fe 2p peaks in Figure 2H confirm the presence of Fe^{3+} ions with characteristic binding energies of 708.46 and 721.4 eV[25]. Figure 2I depicts the transmission spectra and UV-vis absorption spectra of TiO_2 and TiO_2/In_2S_3 prepared with various amounts of indium nitrate. All samples exhibit pronounced UV absorbance, and with an increasing amount of indium nitrate, the light absorption range of TiO_2/In_2S_3 progressively extends into the visible light region. The photographs of TiO_2 and TiO_2/In_2S_3 photoanodes in Supplementary Figure 4A can directly confirm the improved visible light absorption. This demonstrates that the In_2S_3 layer can effectively enhance the visible light absorption for more electron-hole pairs photogeneration.

PEC performance of TiO_2/In_2S_3/NFP photoanode

In_2S_3 and NFP serve a light absorption layer and cocatalyst layer, respectively, which can greatly influence the PEC performance of the TiO_2/In_2S_3/NFP photoanode. The amount of indium nitrate and the reaction time and temperature of NFP growth were optimized first in this work. For the following experiments,

0.05 mmol $In(NO_3)_3$, 3 h NFP growth time, and 60 °C NFP synthesis temperature were ascertained. The detailed optimization results are shown in Supplementary Figures 5-8.

PEC performances of the TiO_2/In_2S_3/NFP photoanode are shown in Figure 3, compared with the control photoanodes of TiO_2 and TiO_2/In_2S_3. In Figure 3A, the photocurrent density of TiO_2/In_2S_3/NFP is 1.81 mA cm^{-2}, which is five times higher than that of TiO_2 (0.30 mA cm^{-2}). The TiO_2/In_2S_3 heterojunction exhibits a photocurrent density of 1.3 mA cm^{-2}. This clearly demonstrates the critical role of TiO_2/In_2S_3 heterojunction fabrication. The applied bias photon-to-current efficiency (ABPE) was further calculated based on the light LSV curves, and the results are depicted in Figure 3B. TiO_2/In_2S_3/NFP has the highest ABPE efficiency of 0.94% at 0.51 V *vs.* RHE, surpassing the as-prepared TiO_2 by 5.8 times. As shown in Figure 3C, the normalized photovoltage decay curves show that the TiO_2/In_2S_3/NFP photoanode attenuates the fastest under dark conditions. This suggests an improved separation of photogenerated electron-hole pairs[40]. Additionally, the photovoltage of TiO_2/In_2S_3/NFP is around 130 mV higher than that of the as-prepared TiO_2. The photovoltage was obtained by calculating the difference between OCP_{dark} and OCP_{light}. The photovoltage value can reflect the degree of energy band bending at the semiconductor-electrolyte interface (SEI). A larger photovoltage indicates a more pronounced energy band bending and a stronger built-in electric field generated by the SEI[41], which can enhance the charge separation. Figure 3D illustrates the I-t curves under the chopped light, which can reflect the transient photocurrent response of photoanodes. Notably, no discernible transient peak can be observed, suggesting the effective separation of the photogenerated electrons and holes[42]. The origin of the photocurrent decay is believed to be due to the poor charge transport of TiO_2/In_2S_3/NFP, which may be changed by doping TiO_2. The inset of Figure 3D illustrates that the transient decay time (τ) becomes longer after the formation of TiO_2/In_2S_3 heterojunction and the NFP modification. The increased τ of TiO_2/In_2S_3/NFP indicates that the charge recombination has been suppressed efficiently[43]. Dark LSV curves of TiO_2, TiO_2/In_2S_3, and TiO_2/In_2S_3/NFP electrodes are shown in Supplementary Figure 9. At the current density of 10 mA cm^{-2}, the overpotential of TiO_2/In_2S_3/NFP is significantly negative shift by 166 mV compared to TiO_2/In_2S_3. This confirms the role of NFP overlayer as cocatalyst for water oxidation reaction.

To reveal the PEC stability of TiO_2/In_2S_3/NFP, a long-term stability test was performed nonstop for 12 h under AM1.5G illumination at 1.23 V *vs.* RHE, as depicted in Figure 3E. After 12 h, TiO_2/In_2S_3/NFP exhibits an approximate 95% retention of photocurrent after an initial transient decrease, which is an 11% improvement over TiO_2/In_2S_3 (84%). The high stability of TiO_2/In_2S_3/NFP should be attributed to the robust NFP, which can also block the photocorrosion of In_2S_3 by physically separating the semiconductor from the electrolyte. The slight decrease of TiO_2/In_2S_3/NFP should be attributed to the imperfect coating of NFP on the surface of TiO_2/In_2S_3. It is worth noting that the photocurrent of TiO_2/In_2S_3/NFP shows significant improvement from 1.81 to 3.1 mA cm^{-2} through the LSV measurements [Supplementary Figure 10]. As shown in Supplementary Figure 10C, ECSA was used as a key indicator for evaluating the catalytic performance of photoanodes[44]. After the stability test, TiO_2/In_2S_3/NFP (5.06×10^{-2} mF cm^{-2}) is 1.57 times the as-prepared photoanode (3.22×10^{-2} mF cm^{-2}). This increase is consistent with the improvement of photocurrent, illustrating that the photocurrent enhancement is due to the enhanced ECSA of TiO_2/In_2S_3/NFP[45]. This is consistent with the reported light-induced restorative effect of the Prussian blue material[33]. The inherent mechanism should be further investigated for answering this open question. The morphology and XPS characterizations of the tested TiO_2/In_2S_3 and TiO_2/In_2S_3/NFP photoanodes were performed, and the results are shown in Supplementary Figure 11 and the inset of Figure 3E. The NFP overlayer can greatly slow down the photocorrosion of In_2S_3. After the stability test, the Ni 2p peaks of TiO_2/In_2S_3/NFP are similar to the peaks of $Ni(OH)_2$[46]. This suggests that the as-prepared NFP cocatalyst is partially transformed into the active species of $Ni(OH)_2$, which is consistent with the reported results[47]. As per the previous findings,

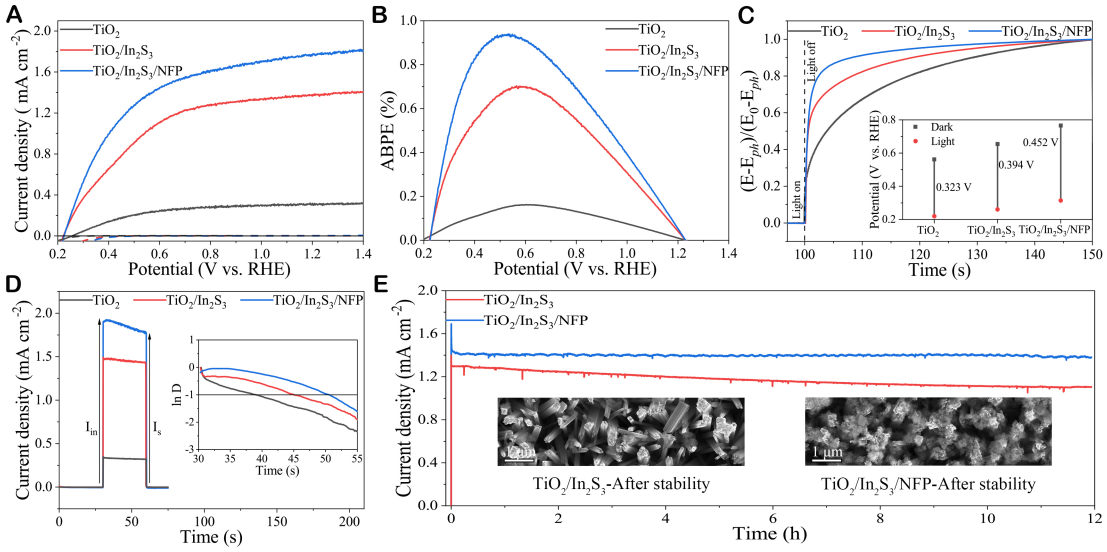

Figure 3. (A) LSV curves, (B) ABPE plots, (C) normalized photovoltage decay and inset OCP, (D) transient photocurrent curves and inset transient decay time (τ) curves of TiO_2, TiO_2/In_2S_3, and TiO_2/In_2S_3/NFP. (E) PEC stability curves of TiO_2/In_2S_3 and TiO_2/In_2S_3 /NFP photoanodes at 1.23 V *vs.* RHE under AM1.5G illumination. Inset: SEM images of the tested TiO_2/In_2S_3 and TiO_2/In_2S_3/NFP photoanodes.

the *in-situ* generated $Ni(OH)_2$ from NFP can create $NiOOH_{2-x}$ that contains Ni^{4+} ions, which are highly active sites for water oxidation reactions. In addition, Supplementary Table 1 summarizes the comparison of the PEC performance of this work with the reported related photoanodes. The PEC performance of TiO_2/In_2S_3 achieved in this study is comparable to or surpassing that of the reported photoanodes. This work further demonstrates the effectiveness of NFP as a cocatalyst for TiO_2-based photoanodes. In the absence of any sacrificial agents, the photocurrent density of the TiO_2/In_2S_3/NFP photoanode reaches 1.81 mA cm^{-2}, which is six times that of the bare TiO_2. In addition, we measured the photocurrent of TiO_2, TiO_2/In_2S_3, and TiO_2/In_2S_3/NFP photoanodes under various light intensities, such as 40, 70, 100, 130, 160, 190, and 200 mW cm^{-2}. There is a linear growth of the photocurrent with the light intensity in the measured range [Supplementary Figure 12]. Moreover, TiO_2/In_2S_3 and TiO_2/In_2S_3/NFP photoanodes show a higher slope of ~0.02 mA mW^{-1} than that of TiO_2 (0.004 mA mW^{-1}). This feature suggests that the TiO_2/In_2S_3 heterojunction and the NFP cocatalyst overlayer can effectively facilitate the charge separation without limiting the hole transfer to the electrolyte[48].

The ECSA of TiO_2, TiO_2/In_2S_3, and TiO_2/In_2S_3/NFP was further studied. CV curves [Supplementary Figure 13] were measured at scan rates of 5-100 mV s^{-1} in 1 M KOH, within a potential window of 0.625-0.725 V *vs.* RHE. The relationship between ΔJ and scan rate is illustrated in Figure 4A. The fitted dashed line provides the double-layer capacitance of TiO_2-based photoanodes, determined by their slopes. After the coating of the NFP overlayer, the TiO_2/In_2S_3/NFP photoanode presents a two-fold ECSA in comparison with TiO_2. This increase is lower than the improvement of five times on the photocurrent. This implies a significantly synergistic effect among TiO_2, In_2S_3, and NFP, not just the increase of ECSA. In order to investigate the charge transfer processes at the SEI interface, we conducted PEIS experiments under AM1.5G illumination at 0.47 V *vs.* RHE. The Nyquist plot was fitted using an equivalent circuit model, as shown in the inset of Figure 4B. It consists of a series resistance (R_s), a trapping resistance (R_{trap}), a bulk phase constant phase element (CPE_{bulk}), a charge transfer resistance ($R_{ct,trap}$), and a trapping CPE (CPE_{trap}). The fitting parameters used are summarized in Table 1. Compared with TiO_2/In_2S_3, the TiO_2/In_2S_3/NFP photoanode shows a significant decrease in R_{trap} (475.15 Ω) and $R_{ct,trap}$ (5711 Ω). This demonstrates that the

Table 1. Electrical element parameters of TiO_2-based photoanodes extracted from PEIS after the equivalent circuit model fitting

Photoanode	R_s (Ω)	R_{trap} (Ω)	CPE_{bulk} (F)	$R_{ct,trap}$ (Ω)	CPE_{trap} (F)
TiO_2	19.48	863.74	4.37E−7	15,472	2.61E−5
TiO_2/In_2S_3	18.79	857.52	4.23E−7	13,515	1.13E−5
TiO_2/In_2S_3/NFP	8.48	475.15	1.61E−7	5,711	1.41E−5

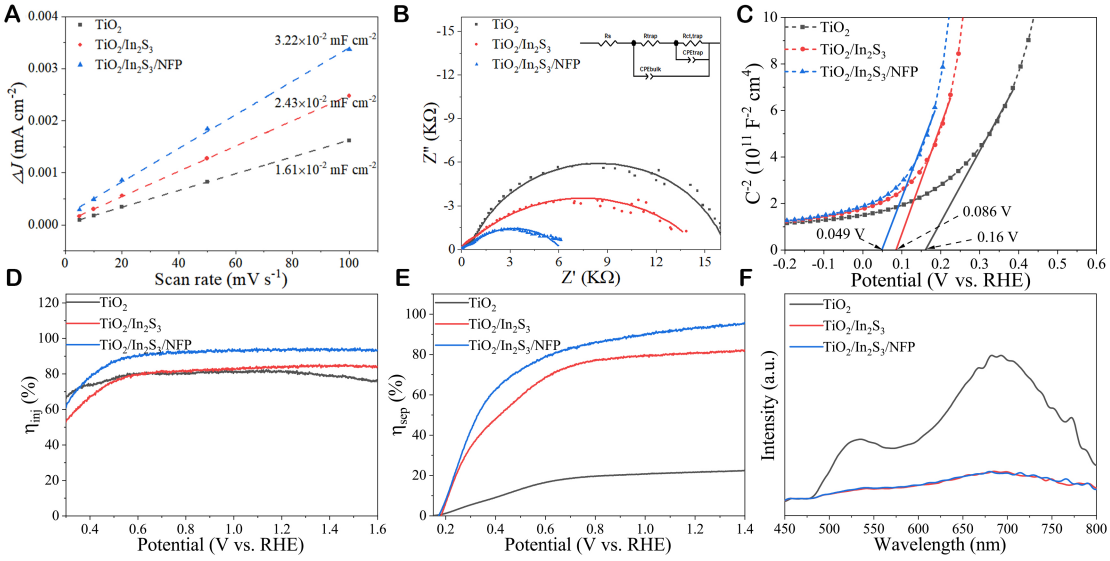

Figure 4. (A) Determination of capacitance (C_{dl}) values through ΔJ *vs.* scan rate plots for TiO_2, TiO_2/In_2S_3, and TiO_2/In_2S_3/NFP. (B) Nyquist plots of TiO_2-based photoanodes measured at 0.47 V *vs.* RHE under AM1.5G illumination. Inset shows the equivalent circuit for alternating current (AC) impedance fitting. (C) M-S plots of TiO_2-based photoanodes measured at a fixed frequency of 2,000 Hz in the dark. (D) Surface charge injection efficiency (η_{inj}) of TiO_2-based photoanodes. (E) Bulk charge separation efficiency (η_{sep}) of TiO_2-based photoanodes. (F) PL spectra of TiO_2, TiO_2/In_2S_3, and TiO_2/In_2S_3/NFP.

NFP cocatalyst layer can boost the charge transfer kinetics at SEI. M-S plots were acquired at a fixed frequency of 2,000 Hz in the dark, as depicted in Figure 4C. All samples exhibit the positive slopes, illustrating their n-type conductivity. Evidently, TiO_2/In_2S_3/NFP exhibits a more negative flatband potential, indicating the position of the Fermi level of the photoanode in relation to the potential of the reference electrode. The negatively shifted flatband potential is typically associated with a lowered Fermi level[49]. The donor density of TiO_2/In_2S_3/NFP is 1.33 times of that of TiO_2/In_2S_3, indicating the good conductivity of the NFP overlayer for charge transport. To further elucidate the kinetics of the TiO_2-based photoanodes, we measured charge transfer efficiency (η_{inj}) and charge separation efficiency (η_{sep}), as shown in Figure 4D and E, respectively. At 1.23 V *vs.* RHE, TiO_2/In_2S_3/NFP exhibits the highest η_{inj} of 93.86% and the highest η_{sep} of 93.55%. TiO_2/In_2S_3 has a moderate η_{inj} and η_{sep}, corresponding to 84.58% and 80.67%, respectively. TiO_2 only achieves a very low η_{sep} of 21.80%, indicating that the TiO_2/In_2S_3 heterojunction plays a major role for the charge separation. The NFP cocatalyst overlayer can promote the charge injection at SEI and then facilitate the charge separation in the depletion region. Steady-state PL spectra of TiO_2-based photoanodes measured with a light excitation of 420 nm are shown in Figure 4F. PL spectra reveal the radiative recombination of the photogenerated electrons and holes. The PL peaks located at 535.61 and 682.07 nm can be attributed to the excitonic PL process, in which the radiative transition from the sub-bands to the VB top occurs[50]. The sub-bands mainly result from the surface defects of the TiO_2 photoanode. Therefore, the suppressed PL signal can be observed after the formation of TiO_2/In_2S_3 heterojunction. The heterojunction can efficiently boost the process of the charge separation because of the

built-in electric field. The modification of the NFP overlayer cannot further suppress the PL signal. This is because the PL measurements were conducted in air, not in the electrolyte. The charges transferred to the NFP overlayer cannot be migrated from NFP to the redox substance in the air. In other words, in the electrolyte, the NFP overlayer can migrate the charges from NFP to water molecules and promote the charge separation.

Probable mechanism of PEC improvement

To determine the energy band positions of TiO_2 and In_2S_3, Tauc plots were generated using UV-vis absorption spectra [Figure 5A]. UPS spectra of TiO_2 and In_2S_3 were further measured to determine the work functions and the edge of the VB. During the UV-vis absorption spectra and UPS measurements of In_2S_3, the In_2S_3 powder, which was collected from the hydrothermal residues, was used. The photograph of the In_2S_3 powder is shown in Supplementary Figure 4B. The bandgaps (E_g) of TiO_2 and In_2S_3 can be derived from the Tauc plots, corresponding to 3.01 and 1.92 eV, respectively. The two bandgap values are consistent with the reported results[20]. The work functions of 4.39 eV for TiO_2 and 4.08 eV for In_2S_3 can be obtained from the UPS spectra in Figure 5B and C, respectively. Furthermore, the energies from the VB edge to the Fermi level are 2.78 and 1.61 eV for TiO_2 and In_2S_3, respectively. These experimental data offer detailed insights into the energy band structures of TiO_2 and In_2S_3, benefitting our understanding of the electron structure and PEC processes of the TiO_2/In_2S_3 photoanode.

The schematic diagram of the energy band structure before and after the contact between TiO_2 and In_2S_3 [Figure 5D] illustrates that, initially, there is a disparity in the Fermi levels between TiO_2 and In_2S_3, with In_2S_3 exhibiting a higher Fermi level. When In_2S_3 was grown on the surface of TiO_2, electrons began to migrate from In_2S_3 to TiO_2, gradually aligning the Fermi levels of both materials. Finally, a classical type-II heterojunction was formed with TiO_2 and In_2S_3. An internal built-in electric field was generated at the interface of TiO_2/In_2S_3 heterojunction. The electric field direction is from TiO_2 to In_2S_3. The energy band structure of TiO_2/In_2S_3 type-II heterojunction facilitates the separation of the photogenerated charges due to the electric field force. Specifically, it is energy-favorable that the photogenerated electrons are transported from the conduction band (CB) of In_2S_3 to the CB of TiO_2. For the photogenerated holes, the large VB offset at the interface of TiO_2/In_2S_3 can provide tremendous driving force and push the holes to the side of In_2S_3. The separated holes can be migrated to the NFP cocatalyst overlayer. The NFP catalyst captured holes rapidly, preventing the recombination of electrons and holes at the TiO_2/In_2S_3 interface and thus enhancing the utilization of photogenerated charge carriers. More importantly, the NFP catalyst can promote the hole participation in the water oxidation reaction at SEI[16]. As shown in Supplementary Figure 14, the NFP cocatalyst can remarkably improve the electrochemical activity and provide the active species through the state variation of nickel and iron elements. Therefore, thanks to the type-II heterojunction of TiO_2/In_2S_3 and the efficient NFP cocatalyst, a higher photocurrent density can be achieved with TiO_2/In_2S_3/NFP photoanodes. The theoretical photocurrent density (2.03 mA cm^{-2}) of TiO_2/In_2S_3/NFP can be estimated from its UV-vis absorption spectrum shown in Supplementary Figure 15. The experimental photocurrent of 1.81 mA cm^{-2} is ~90% of the above theoretical value. In brief, as shown in Figure 5E, TiO_2 and In_2S_3 can absorb the UV and visible light, respectively, and form the type-II heterojunction. The type-II heterojunction can promote the charge separation and suppress the charge recombination due to the built-in electric field at the interface of TiO_2/In_2S_3. A NFP layer, as cocatlyst and protector, can enhance the water oxidation reactions through the transition of Ni^{2+}/Ni^{3+} and Fe^{2+}/Fe^{3+} and protect the In_2S_3 layer from the photocorrosion, respectively.

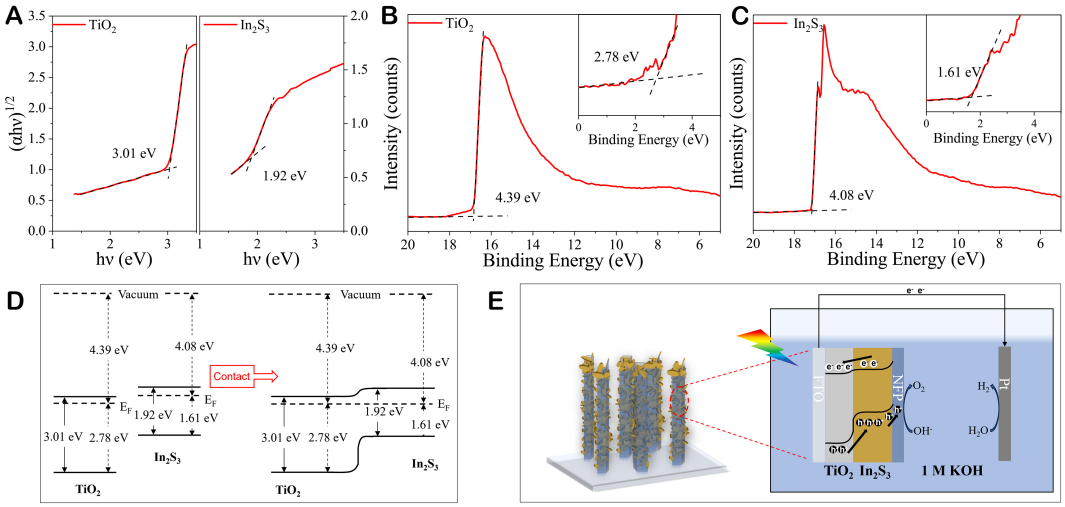

Figure 5. (A) Tauc plots of TiO_2 and In_2S_3. (B) UPS spectrum of TiO_2. (C) UPS spectrum of In_2S_3. (D) Schematic diagrams of the energy band structures for TiO_2 and In_2S_3 before and after their contact. (E) Mechanism diagram of TiO_2/In_2S_3/NFP photoanode for solar water splitting.

CONCLUSIONS

In conclusion, we fabricated a ternary TiO_2/In_2S_3/NFP photoanode by the facile hydrothermal and chemical bath methods. This photoanode achieved a photocurrent density of 1.81 mA cm^{-2} at the potential of 1.23 V *vs.* RHE, reaching around 90% of the theoretical maximum value. Its charge injection efficiency and charge separation efficiency are near 95%. Compared with a pristine TiO_2 photoanode, the kinetics of the TiO_2/In_2S_3/NFP photoanode was significantly improved, such as a low charge transfer resistance, and a suppressed PL signal. The TiO_2/In_2S_3 type-II heterojunction significantly suppresses the charge recombination at the surface of TiO_2 and facilitates the separation of electron-hole pairs under the assistance of the built-in electric field. The NFP cocatalyst overlayer substantially decreases the charge transfer resistance, and promotes the catalytic activity for water oxidation reactions, thereby further improving the PEC performance of TiO_2/In_2S_3. Moreover, the NFP can protect the In_2S_3 layer from the photocorrosion in the electrolyte. Therefore, the synergistic effect of the TiO_2/In_2S_3 heterojunction and NFP cocatalyst determines the finally good PEC performance of the TiO_2/In_2S_3/NFP photoanode. These findings provide some critical insights for the interface engineering and material design in PEC systems.

DECLARATIONS

Authors' contributions

Conceptualization, methodology, investigation, data curation, formal analysis, writing-original draft: Zhang M

Conceptualization, methodology, investigation, formal analysis, funding acquisition, supervision, writing-review and editing: Yang P, Xie J

Methodology, investigation, formal analysis: Tao W, Pang X, Su Y, Peng P, Zheng L, Li R, Wang S, Huang J, Zou L

Availability of data and materials

The data are made available upon request to authors.

Financial support and sponsorship

This work was supported by the Sichuan Science and Technology Program (2022NSFSC1272), the Scientific Research Starting Project of SWPU (2021QHZ018), the Chengdu Education Bureau Program (QYGG004, QYGG010), the School of New Energy and Materials Program (2022SCNYTZHCL013), and the

Production-Education Integration Demonstration Project of Sichuan Province "Photovoltaic Industry Production-Education Integration Comprehensive Demonstration Base of Sichuan Province (Sichuan Financial Education [2022] No.106)".

Conflicts of interest

All authors declared that there are no conflicts of interest.

Ethical approval and consent to participate

Not applicable.

Consent for publication

Not applicable.

Copyright

REFERENCES

1. Ta XMC, Daiyan R, Nguyen TKA, Amal R, Tran-Phu T, Tricoli A. Alternatives to water photooxidation for photoelectrochemical solar energy conversion and green H_2 production. *Adv Energy Mater* 2022;12:2201358. DOI
2. Yang Y, Li P, Zheng X, et al. Anion-exchange membrane water electrolyzers and fuel cells. *Chem Soc Rev* 2022;51:9620-93. DOI
3. Shi X, Jeong H, Oh SJ, et al. Unassisted photoelectrochemical water splitting exceeding 7% solar-to-hydrogen conversion efficiency using photon recycling. *Nat Commun* 2016;7:11943. DOI PubMed PMC
4. Takata T, Jiang J, Sakata Y, et al. Photocatalytic water splitting with a quantum efficiency of almost unity. *Nature* 2020;581:411-4. DOI
5. Guo Q, Zhou C, Ma Z, Yang X. Fundamentals of TiO_2 photocatalysis: concepts, mechanisms, and challenges. *Adv Mater* 2019;31:e1901997. DOI PubMed
6. Guo Y, Zhang R, Zhang S, et al. Pd doping-weakened intermediate adsorption to promote electrocatalytic nitrate reduction on TiO_2 nanoarrays for ammonia production and energy supply with zinc-nitrate batteries. *Energy Environ Sci* 2021;14:3938-44. DOI
7. Wu J, Yang X, Zhang J, et al. Surface engineering of Ni_2P/CoP nanosheet heterojunctions by the formation of F-doped carbon layers for boosting urea-rich water electrolysis. *J Power Sources* 2022;548:232065. DOI
8. Sun C, Shao Z, Hu Y, Peng Y, Xie Q. Photoelectrocatalysis synthesis of ammonia based on a Ni-doped MoS_2/Si nanowires photocathode and porous water with high N_2 solubility. *ACS Appl Mater Interfaces* 2023;15:23085-92. DOI PubMed
9. Zhang J, Yu L, Chen Y, Lu XF, Gao S, Lou XWD. Designed formation of double-shelled Ni-Fe layered-double-hydroxide nanocages for efficient oxygen evolution reaction. *Adv Mater* 2020;32:e1906432. DOI
10. Xu H, Liao Y, Gao Z, Qing Y, Wu Y, Xia L. A branch-like Mo-doped Ni_3S_2 nanoforest as a high-efficiency and durable catalyst for overall urea electrolysis. *J Mater Chem A* 2021;9:3418-26. DOI
11. Tong W, Huang B, Wang P, Shao Q, Huang X. Exposed facet-controlled N_2 electroreduction on distinct Pt_3Fe nanostructures of nanocubes, nanorods and nanowires. *Natl Sci Rev* 2021;8:nwaa088. DOI PubMed PMC
12. Zheng J, Sun L, Jiao C, et al. Hydrothermally synthesized Ti/Zr bimetallic MOFs derived N self-doped TiO_2/ZrO_2 composite catalysts with enhanced photocatalytic degradation of methylene blue. *Colloid Surface A* 2021;623:126629. DOI
13. Zhang Q, Sun M, Yao M, et al. Interfacial engineering of an FeOOH@Co_3O_4 heterojunction for efficient overall water splitting and electrocatalytic urea oxidation. *J Colloid Interface Sci* 2022;623:617-26. DOI
14. Qian Z, Zhang R, Xiao Y, et al. Trace to the source: self-tuning of MOF photocatalysts. *Adv Energy Mater* 2023;13:2300086. DOI
15. Chen L, Song XL, Ren JT, Yuan ZY. Precisely modifying Co_2P/black TiO_2 S-scheme heterojunction by in situ formed P and C dopants for enhanced photocatalytic H_2 production. *Appl Catal B Environ* 2022;315:121546. DOI
16. Wang L, Tang G, Liu S, et al. Interfacial active-site-rich 0D Co_3O_4/1D TiO_2 p-n heterojunction for enhanced photocatalytic hydrogen evolution. *Chem Eng J* 2022;428:131338. DOI
17. Li J, Du X, Zhang X, Wang Z. Fe_7Se_8@Fe_2O_3 heterostructure nanosheets as bifunctional electrocatalyst for urea electrolysis. *Int J Hydrog Energy* 2022;47:35203-14. DOI
18. Kupfer B, Majhi K, Keller DA, et al. Thin film Co_3O_4/TiO_2 heterojunction solar cells. *Adv Energy Mater* 2015;5:1401007. DOI
19. Zhou C, Li J, Wang J, et al. Efficient H_2 production and TN removal for urine disposal using a novel photoelectrocatalytic system of Co_3O_4/$BiVO_4$ - $MoNiCuO_x$/Cu. *Appl Catal B Environ* 2023;324:122229. DOI
20. Park J, Lee TH, Kim C, et al. Hydrothermally obtained type-II heterojunction nanostructures of In_2S_3/TiO_2 for remarkably enhanced photoelectrochemical water splitting. *Appl Catal B Environ* 2021;295:120276. DOI
21. Fan W, Chen C, Bai H, Luo B, Shen H, Shi W. Photosensitive polymer and semiconductors bridged by Au plasmon for

photoelectrochemical water splitting. *Appl Catal B Environ* 2016;195:9-15. DOI

22. Tao Y, Ma Z, Wang W, et al. Nickel phosphide clusters sensitized TiO_2 nanotube arrays as highly efficient photoanode for photoelectrocatalytic urea oxidation. *Adv Funct Mater* 2023;33:2211169. DOI
23. Cui W, Bai H, Shang J, et al. Organic-inorganic hybrid-photoanode built from NiFe-MOF and TiO_2 for efficient PEC water splitting. *Electrochim Acta* 2020;349:136383. DOI
24. Tang P, Han L, Hegner FS, et al. Boosting photoelectrochemical water oxidation of hematite in acidic electrolytes by surface state modification. *Adv Energy Mater* 2019;9:1901836. DOI
25. Yang X, Kang L, Wei Z, et al. A self-sacrificial templated route to fabricate CuFe Prussian blue analogue/$Cu(OH)_2$ nanoarray as an efficient pre-catalyst for ultrastable bifunctional electro-oxidation. *Chem Eng J* 2021;422:130139. DOI
26. Hegner FS, Herraiz-Cardona I, Cardenas-Morcoso D, López N, Galán-Mascarós JR, Gimenez S. Cobalt hexacyanoferrate on $BiVO_4$ photoanodes for robust water splitting. *ACS Appl Mater Interfaces* 2017;9:37671-81. DOI PubMed PMC
27. Moss B, Hegner FS, Corby S, et al. Unraveling charge transfer in CoFe Prussian blue modified $BiVO_4$ photoanodes. *ACS Energy Lett* 2019;4:337-42. DOI
28. Hegner FS, Cardenas-Morcoso D, Giménez S, López N, Galan-Mascaros JR. Level alignment as descriptor for semiconductor/catalyst systems in water splitting: the case of hematite/cobalt hexacyanoferrate photoanodes. *ChemSusChem* 2017;10:4552-60. DOI PubMed
29. Feng L, Li N, Tang S, Guo Y, Zheng J, Li X. Photoelectrochemical performance of titanium dioxide/Prussian blue analogue synthesized by impregnation conversion method as photoanode. *Inorg Chem Commun* 2021;125:108349. DOI
30. Pal D, Maity D, Sarkar A, De D, Raj A, Khan GG. Multifunctional ultrathin amorphous CoFe-Prussian blue analogue catalysts for efficiently boosting the oxygen evolution activity of antimony-doped TiO_2 nanorods photoanode. *ACS Appl Energy Mater* 2022;5:15000-9. DOI
31. Khan AZ, Kandiel T, Abdel-Azeim S, Jahangir TN, Alhooshani K. Phosphate ions interfacial drift layer to improve the performance of CoFe-Prussian blue hematite photoanode toward water splitting. *Appl Catal B Environ* 2022;304:121014. DOI
32. Usman E, Barzgar Vishlaghi M, Sadigh Akbari S, Karadaş F, Kaya S. Hybrid CuFe-CoFe Prussian blue catalysts on $BiVO_4$ for enhanced charge separation and injection for photoelectrochemical water oxidation. *ACS Appl Energy Mater* 2022;5:15434-41. DOI
33. Shaddad MN, Arunachalam P, Labis J, Hezam M, Al-Mayouf AM. Fabrication of robust nanostructured (Zr)$BiVO_4$/nickel hexacyanoferrate core/shell photoanodes for solar water splitting. *Appl Catal B Environ* 2019;244:863-70. DOI
34. Bai S, Jia S, Zhao Y, et al. NiFePB-modified ZnO/$BiVO_4$ photoanode for PEC water oxidation. *Dalton Trans* 2023;52:5760-70. DOI
35. Lee BR, Jang HW. β-In_2S_3 as water splitting photoanodes: promise and challenges. *Electron Mater Lett* 2021;17:119-35. DOI
36. Wang X, Xie J, Li CM. Architecting smart "umbrella" Bi_2S_3/rGO-modified TiO_2 nanorod array structures at the nanoscale for efficient photoelectrocatalysis under visible light. *J Mater Chem A* 2015;3:1235-42. DOI
37. Zhu C, Yao H, Le S, et al. S-scheme photocatalysis induced by ultrathin TiO_2(B) nanosheets-anchored hierarchical In_2S_3 spheres for boosted photocatalytic activity. *Compos Part B Eng* 2022;242:110082. DOI
38. Nawaz R, Kait CF, Chia HY, et al. Manipulation of the Ti^{3+}/Ti^{4+} ratio in colored titanium dioxide and its role in photocatalytic degradation of environmental pollutants. *Surf Interfaces* 2022;32:102146. DOI
39. Li J, Zhang M, Guan Z, Li Q, He C, Yang J. Synergistic effect of surface and bulk single-electron-trapped oxygen vacancy of TiO_2 in the photocatalytic reduction of CO_2. *Appl Catal B Environ* 2017;206:300-7. DOI
40. Pu YC, Ling Y, Chang KD, et al. Surface passivation of TiO_2 nanowires using a facile precursor-treatment approach for photoelectrochemical water oxidation. *J Phys Chem C* 2014;118:15086-94. DOI
41. Wu F, Xie J, You Y, et al. Cobalt metal-organic framework ultrathin cocatalyst overlayer for improved photoelectrochemical activity of Ti-doped hematite. *ACS Appl Energy Mater* 2020;3:4867-76. DOI
42. Ren J, Yang P, Wang L, et al. In situ transition of a nickel metal-organic framework on TiO_2 photoanode towards urea photoelectrolysis. *Catalysts* 2023;13:727. DOI
43. Sharma MD, Basu M. Nanosheets of In_2S_3/S-C_3N_4-dots for solar water-splitting in saline water. *Langmuir* 2022;38:12981-90. DOI PubMed
44. Wu L, Yu L, Zhang F, et al. Heterogeneous bimetallic phosphide Ni_2P-Fe_2P as an efficient bifunctional catalyst for water/seawater splitting. *Adv Funct Mater* 2021;31:2006484. DOI
45. Xie J, Qu H, Lei F, et al. Partially amorphous nickel-iron layered double hydroxide nanosheet arrays for robust bifunctional electrocatalysis. *J Mater Chem A* 2018;6:16121-9. DOI
46. Grosvenor AP, Biesinger MC, Smart RS, Mcintyre NS. New interpretations of XPS spectra of nickel metal and oxides. *Surf Sci* 2006;600:1771-9. DOI
47. Su X, Wang Y, Zhou J, Gu S, Li J, Zhang S. Operando spectroscopic identification of active sites in NiFe Prussian blue analogues as electrocatalysts: activation of oxygen atoms for oxygen evolution reaction. *J Am Chem Soc* 2018;140:11286-92. DOI
48. Chen R, Zhang D, Wang Z, et al. Linking the photoinduced surface potential difference to interfacial charge transfer in photoelectrocatalytic water oxidation. *J Am Chem Soc* 2023;145:4667-74. DOI
49. Wang X, Li H, Zhang J, Liu X, Zhang X. Wedged ß- In_2S_3 sensitized TiO_2 films for enhanced photoelectrochemical hydrogen generation. *J Alloys Compd* 2020;831:154798. DOI
50. Liqiang J, Yichun Q, Baiqi W, et al. Review of photoluminescence performance of nano-sized semiconductor materials and its relationships with photocatalytic activity. *Sol Energy Mater Sol Cells* 2006;90:1773-87. DOI